



Head-to-nerve analysis of electromechanical impairments of diffuse axonal injury

Ilaria Cinelli¹ · Michel Destrade² · Peter McHugh¹ · Antonia Trotta³ · Michael Gilchrist³ · Maeve Duffy⁴

Received: 13 December 2017 / Accepted: 20 October 2018
© Springer-Verlag GmbH Germany, part of Springer Nature 2018

Abstract

The aim was to investigate mechanical and functional failure of diffuse axonal injury (DAI) in nerve bundles following frontal head impacts, by finite element simulations. Anatomical changes following traumatic brain injury are simulated at the macroscale by using a 3D head model. Frontal head impacts at speeds of 2.5–7.5 m/s induce mild-to-moderate DAI in the white matter of the brain. Investigation of the changes in induced electromechanical responses at the cellular level is carried out in two scaled nerve bundle models, one with myelinated nerve fibres, the other with unmyelinated nerve fibres. DAI occurrence is simulated by using a real-time fully coupled electromechanical framework, which combines a modulated threshold for spiking activation and independent alteration of the electrical properties for each three-layer fibre in the nerve bundle models. The magnitudes of simulated strains in the white matter of the brain model are used to determine the displacement boundary conditions in elongation simulations using the 3D nerve bundle models. At high impact speed, mechanical failure occurs at lower strain values in large unmyelinated bundles than in myelinated bundles or small unmyelinated bundles; signal propagation continues in large myelinated bundles during and after loading, although there is a large shift in baseline voltage during loading; a linear relationship is observed between the generated plastic strain in the nerve bundle models and the impact speed and nominal strains of the head model. The myelin layer protects the fibre from mechanical damage, preserving its functionalities.

Keywords Coupled electromechanical modelling · Finite element modelling · Equivalences · Diffuse axonal injury · Trauma

Electronic supplementary material The online version of this article (<https://doi.org/10.1007/s10237-018-1086-8>) contains supplementary material, which is available to authorized users.

✉ Ilaria Cinelli
i.cinelli1@nuigalway.ie

Michel Destrade
michel.destrade@nuigalway.ie

Peter McHugh
peter.mchugh@nuigalway.ie

Antonia Trotta
antonia.trotta@ucdconnect.ie

Michael Gilchrist
michael.gilchrist@ucd.ie

Maeve Duffy
maeve.duffy@nuigalway.ie

¹ Discipline of Biomedical Engineering, College of Engineering and Informatics, National University of Ireland Galway, University Road, Galway H91 TK33, Republic of Ireland

1 Introduction

Current research interests in brain modelling aim at understanding head injury (Dixit et al. 2017; Garcia-Gonzalez et al. 2018; Samaka and Tarlochan 2013; Horgan et al. 2003, 2004; Wright 2012; Young et al. 2015), axonal injury (Cinelli et al. 2017a, b, c; Garcia-Grajales et al. 2015; Jérusalem et al. 2014; Mohammadipour et al. 2017; Wright 2012), sport concussions (McCroory et al. 2017), neuronal morphology (Abdellah et al. 2018; Kanari et al. 2018) and brain connectivity (Wazen et al. 2014) when medical conditions are present, such as

- ² School of Mathematics, Statistics and Applied Mathematics, College of Science, National University of Ireland Galway, Galway H91 TK33, Republic of Ireland
- ³ School of Mechanical and Materials Engineering, University College Dublin, Belfield, Dublin 4, Republic of Ireland
- ⁴ Power Electronics Research Centre, Discipline of Electrical and Electronic Engineering, College of Engineering and Informatics, National University of Ireland Galway, University Road, Galway H91 TK33, Republic of Ireland

Alzheimer's disease, depression and epilepsy (Wazen et al. 2014). Brain models vary according to application (Dixit et al. 2017; Samaka and Tarlochan 2013) and can be based on computed tomography and magnetic resonance tomography images (Horgan et al. 2003, 2004) or can be based on magnetic resonance imaging (Garcia-Gonzalez et al. 2017, 2018; Wazen et al. 2014). Accuracy and precision of finite element models of the brain are achieved by design, where the brain anatomy is replicated by the inclusion of a certain number of layers, and where material properties aim to conform to reality (Dixit et al. 2017; Samaka and Tarlochan 2013). However, most macroscale brain models do not account for a detailed representation of the microscale structure of nervous cells to limit the computational cost (Dixit et al. 2017; Samaka and Tarlochan 2013; Mohammadipour et al. 2017; Wright 2012), although cell models have been developed in this regard (Abdellah et al. 2018; Cinelli et al. 2017a, b; Garcia-Grajales et al. 2015; Jérusalem et al. 2014; Kanari et al. 2018; Mohammadipour et al. 2017; Wright 2012). Recent published works of finite element models of nervous cells tend to simulate both the mechanical structure and the functionality of the cell (Cinelli et al. 2017a, b; Garcia-Grajales et al. 2015; Jérusalem et al. 2014; Mohammadipour et al. 2017), as its relevance has been demonstrated in experimental works (Galbraith et al. 1993; El Hady et al. 2015; Mosgaard et al. 2015; Mueller et al. 2014; Zhang et al. 2001).

Traumatic brain injury (TBI) is a common result of head impact. TBI is a major public health problem generated by falls, vehicle accidents, sport injuries, military incidents, etc. (Ma et al. 2016; Wright 2012; Zhang et al. 2014). In Europe, fall-related, work-related, and all injury-related deaths due to TBI are as high as 47.4% (Li et al. 2016), 8.5% (Li et al. 2016) and 37% (Majdan et al. 2016), respectively. Brain injuries are associated with increased mortality and decreased life expectancy compared to the general population (Majdan et al. 2016). Furthermore, people with TBI incur substantial direct (healthcare) and indirect (loss of productivity and care-giver-related) costs (Majdan et al. 2016). Multiple factors, such as individual anatomy, head acceleration, magnitude and direction of forces, protective equipment, explain the high heterogeneity of TBI (Hemphill et al. 2015; Siedler et al. 2014). Neurochemical, metabolic, neuroinflammation, blood perfusion and other molecular-based processes change the mechanobiology and the cellular microenvironment of the brain as a consequence of the localisation of stresses following TBI (Hemphill et al. 2015; Kan et al. 2012). The challenge in understanding the biomechanics of TBI leads to an increase in difficulty in treating and preventing the development of cognitive and behavioural problems (Hemphill et al. 2015; Kan et al. 2012).

Additionally, TBI has effects at the *cellular level*. The neuropathology of TBI includes focal damage of brain tissue or widespread axonal injury (Jérusalem et al. 2014;

Wright 2012). TBI-induced dynamic deformations increase the risk of axonal stretch and shear injuries to axons scattered throughout the brain parenchyma (Lajtha et al. 2009; Wright 2012), generating structural and functional damage (such as leaking nerve membranes (Yu et al. 2012) and cytoskeleton disruption (Hemphill et al. 2015; Smith et al. 1999; Tang-Schomer et al. 2017)), leading to rupture of the axon (Hemphill et al. 2015; Siedler et al. 2014; Smith et al. 1999). Strain and strain rate are known to play important roles in the induced electrophysiological impairments and functional deficits at the axonal level (Boucher et al. 2012; Geddes et al. 2003; Jérusalem et al. 2014).

In particular, mild and severe TBI impacts lead to *Diffuse Axonal Injury* (DAI), which refers to the damage experienced by neural axons in the deep white matter regions of the brain (Ma et al. 2016; Wright 2012). DAI is associated with a high risk of developing future neurodegenerative disease (Hemphill et al. 2015; Kan et al. 2012), and the progressive course of DAI is responsible for long-lasting neurological impairments associated with high rates of mortality (Lajtha et al. 2009; Smith and Meaney 2000; Wang et al. 2010). Currently, no clinical treatments and prognosis can be used against DAI because of the complexity in diagnosis when using medical imaging, due to haemorrhages, haematomas and tissue lesions of the neighbouring injured area (Hemphill et al. 2015; Lajtha et al. 2009; Ma et al. 2016; Wright 2012). In effect, DAI can only be established post-mortem.

Computational models of TBI biomechanics can simulate brain trauma based on the principles of mechanics. By replicating head impact dynamics, they enable a detailed investigation of the mechanical and physiological changes linked to anatomical and functional damage of the brain. Modelling presents itself as a tool that could aid in diagnosis as it allows for the evaluation of mechanical and physiological quantities in the brain tissue that cannot be detected by current medical technology.

With the purpose of enhancing the understanding of electromechanical DAI occurrences, in this work we adopt a multi-scale approach and use two independent models to replicate the anatomical and functional changes induced by TBI events: (1) at the *macroscale*, the induced anatomical changes are simulated by using an advanced 3D biomechanical Head Model [the University College Dublin brain trauma model—UCDBTM (Horgan et al. 2003, 2004)]; (2) at the *microscale*, the structural and functional changes of complex electromechanical impairments at the cellular level are simulated by using a 3D coupled electromechanical nerve bundle model (Cinelli et al. 2017a, c, d). These models replicate the brain macroenvironment and the neural microenvironment, respectively. The sequential use of two independent models is needed to limit the computational cost that would arise from the combined modelling of macro and microfeatures within the same 3D model.

In this paper, we simulate short-term frontal head impacts by using the head model to estimate the deformation of the white matter regions at the instant of impact. Then, the magnitudes of TBI-induced strains in the head model are used to determine the displacement boundary conditions to be applied to the nerve bundle model. The worst-case condition of uniaxial stretching is applied to the fibre bundles, where it has been found that tensile axonal strain is the most realistic mechanism for generating DAI (Bain et al. 2000; Jérusalem et al. 2014; Wright 2012). The variation in the membrane voltage (in terms of its peak and baseline values) is investigated during and after the applied elongation. In this way, electrophysiological and structural occurrences are simulated at the axonal level using realistic TBI elongation simulations. DAI-induced neural strains and voltage changes are analysed using the nerve bundle model in relation to strain levels predicted by the Head Model for different impact speeds.

In the field of head trauma biomechanics, the head model developed at University College Dublin (Horgan et al. 2003) is a 3D finite element (FE) representation of the human head complex, proposed as a tool for the assessment of brain injury mechanisms (Horgan et al. 2003, 2004). The main anatomical features of the UCD head model include the cerebrum, cerebellum and brainstem, intracranial membranes, pia, cerebrospinal fluid layer, dura, a varying thickness three-layered skull (cortical and trabecular bone layers), scalp and the facial bone (Horgan et al. 2003); see Fig. 1. A parametric analysis, undertaken using Abaqus 5.8, was performed to investigate the influence of different mesh densities on the model geometries and material properties (Horgan et al. 2003). The head model consists of a total of 26,913 nodes and 28,287 elements, including linear quadrilateral, hexahedral and triangular elements; see Fig. 1. It has been validated against a series of cadaveric head impact experiments, simulating the Nahum's test (Horgan et al. 2003), and Trosseille's and Hardy et al.'s tests; see account by Horgan et al. (2004). The validation includes both rotational and translational acceleration components (Horgan et al. 2003, 2004). In the current study, we use the head model to simulate frontal head impacts only, where rotations and accelerations are neglected.

Recent experimental evidence of neural activity highlights *complex electromechanical phenomena* happening at the nerve membrane layer (Alvarez et al. 1978; Cinelli et al. 2017a; Galbraith et al. 1993; Geddes et al. 2003; Mueller et al. 2014; Zhang et al. 2001) during signalling (Mosgaard et al. 2015; Zhang et al. 2001). The inclusion of an accurate representation of DAI-related electrophysiological impairments is needed to improve diagnosis, treatment and prognosis of related pathologies (Jérusalem et al. 2014; Lajtha et al. 2009;

Ma et al. 2016; Wright 2012). Our nerve bundle model is a 3D idealised representation of a nerve bundle (Cinelli et al. 2017a, b, c), located in the deep white matter of the brain (Wright 2012); see Fig. 2. The 3D bundle is made of four identical aligned axons whose diameter is within the range of small fibres of the human corpus callosum only (Björnholm et al. 2017), as discussed in (Cinelli et al. 2017a); see Fig. 2. Each fibre is made of extracellular media (ECM), see Fig. 2c; intracellular media (ICM), see Fig. 2e; and a membrane, see Fig. 2d. At the nerve membrane layer, the nerve bundle model includes a fully coupled 3D electromechanical representation of the neural activity, combining piezoelectricity and electrostriction with changes in strain, including total strain (elastic, electrothermal equivalent and plastic strain) (Cinelli et al. 2017a, b). The piezoelectric effect corresponds to a linear variation of the electrical polarisation of a medium linearly with the applied mechanical stress, as seen in nervous cells (Mosgaard et al. 2015; Mueller et al. 2014; Zhang et al. 2001), while electrostriction is a quadratic effect (Alvarez et al. 1978; Mosgaard et al. 2015; Mueller et al. 2014; Zhang et al. 2001) which refers to the displacement of a dielectric under an applied electric field.

We consider the case of two scaled nerve bundle models with a ratio of 2:1, where the nerve fibres inside follow the same ratio, while the thickness of the nerve membrane is maintained constant. The neurite radii of the small bundle (SB) model are: $a_{ICM} = 0.477 \mu\text{m}$, $a_M = 0.480 \mu\text{m}$ and $a_{ECM} = 0.500 \mu\text{m}$ (Cinelli et al. 2015, 2017a, c, d). The neurite radii of the second, bigger bundle (BB) are double those of SB, while the membrane thickness is the same (3 nm). Here, only the cases of a fully unmyelinated bundle or a fully myelinated bundle are considered. In the case of myelinated fibres, the nerve membrane section, see Fig. 2d, is periodically partitioned along the fibre length, similar to the histologic section of a myelinated fibre; see Fig. 1d.1, d.2 (Cinelli et al. 2017a, b). The width of the piecewise conductive membrane regions (or Ranvier's nodes) is $0.002 \mu\text{m}$ and the internode distance is $1 \mu\text{m}$ (Cinelli et al. 2017a, b, c, d, e; Einziger et al. 2003); see Fig. 1d.2. Different electrical properties are assigned to the regions of myelin and Ranvier's node, respectively (Einziger et al. 2003).

This work is a development on the work reported in (Cinelli et al. 2017a, b, c, d). In contrast to (Cinelli et al. 2017a, b, c, d), the boundary conditions used in the nerve bundle model are directly linked to frontal head impacts simulated with the head model. Thus, control over the boundary conditions of both models aims at simulating realistic clinical events, speeding up the transfer of the findings from computational studies to clinical care.

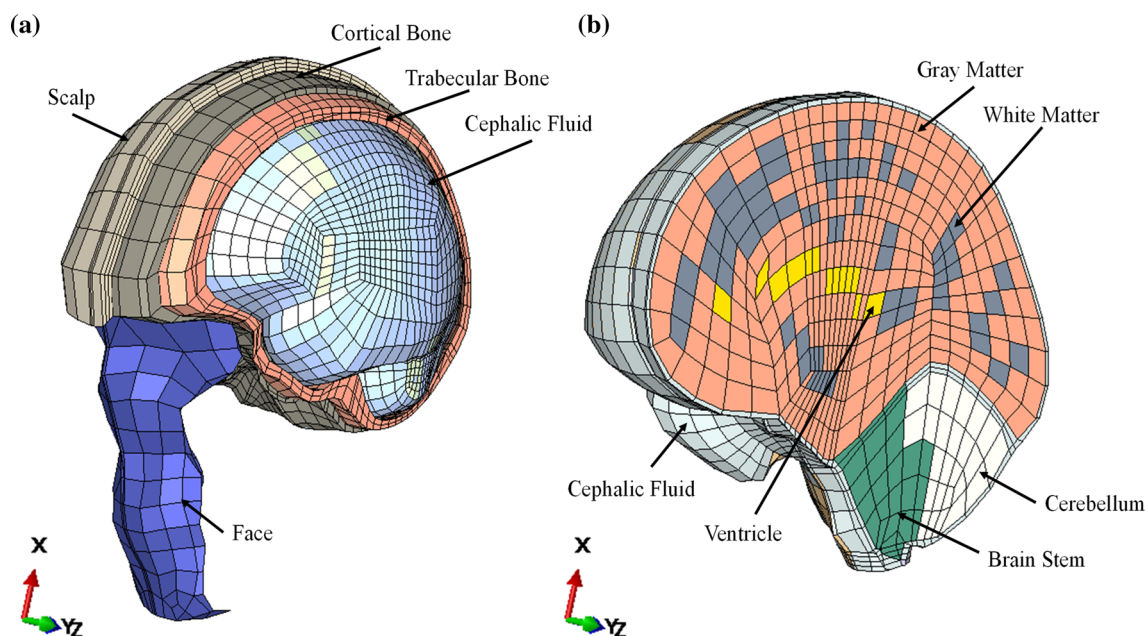


Fig. 1 UCD head model (Horgan et al. 2003, 2004): in **a**, the face, scalp, cortical and trabecular bone, and cephalic fluid; in **b**, grey matter, white matter, cerebellum and brain stem

2 Method

2.1 Boundary conditions

We simulate a frontal impact to induce axonal injuries in the deep white matter of the brain. The Head Model is launched freely with an initial velocity (from 2.5 to 7.5 m/s) against an encastré plane (i.e. the floor) (Horgan et al. 2003). The speed values are within the range of values considered to induce mild and moderate DAI in white matter (Wright 2012). We assume that the loading axis of the velocity impact is aligned parallel to the force of gravity. Since the neck is not included in the model, a free boundary condition is used to simulate a frontal head impact and only short-duration impact responses (<6 ms (Horgan et al. 2003)) are considered (Horgan et al. 2003).

For the nerve bundle model, the encastré boundary condition is applied at the origin of the model at one end, and no rotations are allowed, while a displacement boundary condition is applied at the opposite end (as in uniaxial elongation). Then, an upper-threshold stimulation voltage with a Gaussian distribution is applied on Fibre #3 along its length, see Fig. 2, while the other fibres are activated only if the diffused charges from Fibre #3 generate an input voltage higher than the modulated threshold (Cinelli et al. 2017b, c). The 3D distribution of charges on Fibre #3 modulates the activation of the other fibres; see Fig. 2.

Invoking the *macro-micro*-link, the magnitudes of the displacement boundary conditions of the Nerve Bundle Model are taken from the nominal strain value found in the

white matter regions of the Head Model following impact. Frequency-independent loading conditions are considered throughout, after an initial steady-state interval (lasting about 2 ms). The mechanical loads are applied to the Nerve Bundle Model from 2 to 67 ms, as instantaneous loading conditions, and the model is set to run for 140 ms so that the effects of plasticity can be observed post-loading.

2.2 Material properties

Details of the head model formulation and material properties can be found in the papers by Horgan et al. (2003, 2004), but to summarise, the model utilises linear viscoelasticity combined with hyperelasticity and large deformation kinematics to represent the brain tissue.

For the nerve bundle model, we assume incompressible rate-independent isotropic mechanical behaviour (El Hady et al. 2015), as described in Cinelli et al. (2017a, c, d). Further, we include plasticity, by assuming the same isotropic plastic behaviour for the nerve membrane, ICM, and myelin layer. The yield stress is calculated with an engineering strain equal to 21% (Bain et al. 2000) and a Young's modulus equal to 1 GPa (El Hady et al. 2015). Strain hardening is assumed to occur up to a strain of 65% (Smith et al. 1999). Thus, the engineering strain and engineering stress values are (0.21, 0.21 GPa) and (0.65, 0.65 GPa) for the yield strain limit and strain hardening, respectively. Beyond 65% strain, the stresses are assumed to be constant.

The electrical model parameters for unmyelinated and myelinated fibres are taken from Cinelli et al. (2015, 2017c)

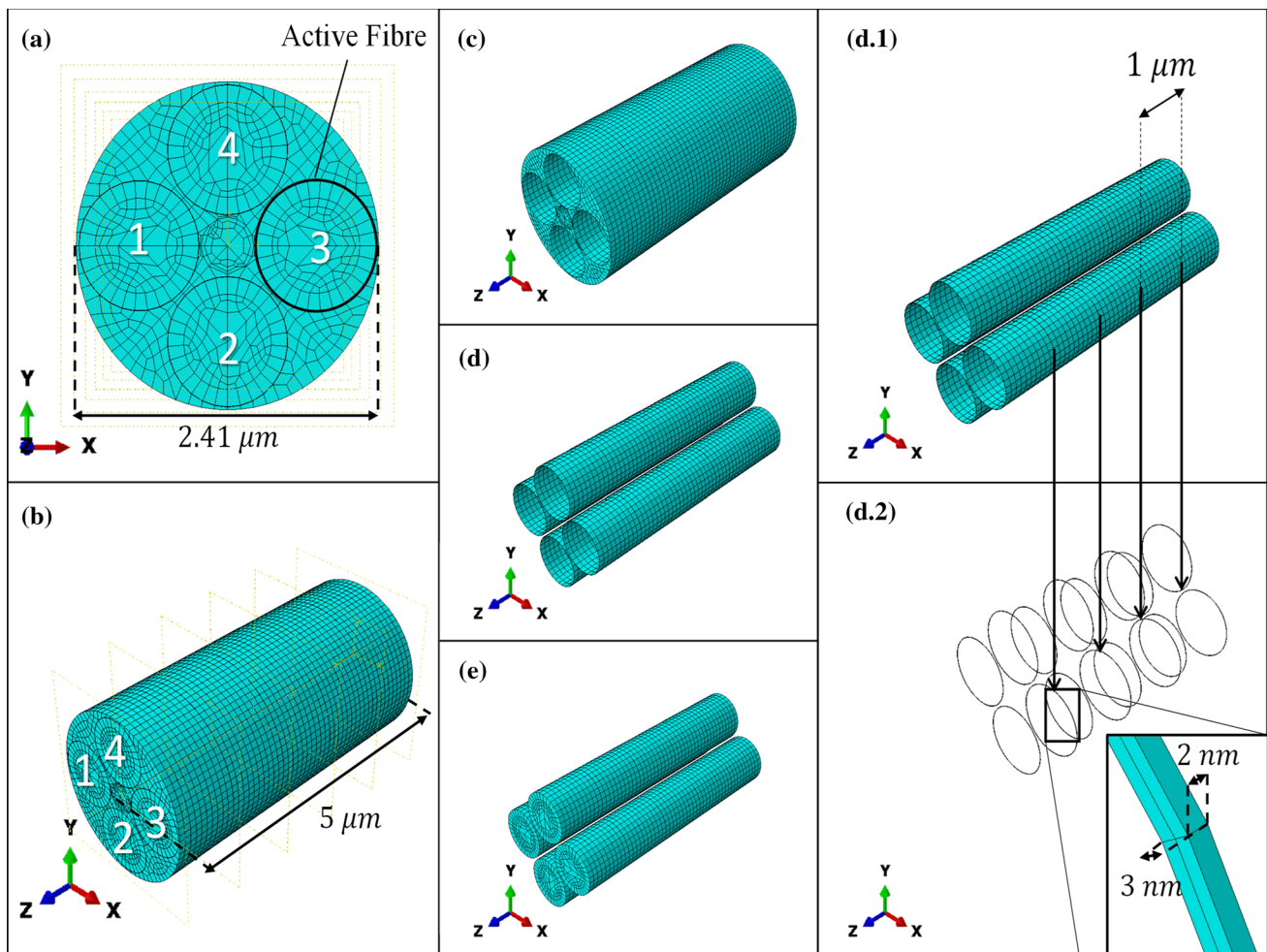


Fig. 2 **a** Frontal view and **b** isometric view of the three-layer nerve bundle made of four fibres. Fibre #3 is the active fibre, i.e. the fibre activated by a Gaussian voltage distribution (El Hady et al. 2015). Fibres #1, #2 and #4 are activated by the charges diffusing from Fibre #3. **c** the ECM; **d** the membrane; **e** the ICM. In the case of myelinated fibres, the membrane layer is periodically partitioned along the fibre length to model

the insulation sheath of the myelin layer, see **d.1**, and the Ranvier node, see **d.2**. The myelin layer length is $1 \mu\text{m}$ and the Ranvier node length is 2 nm , while the radial thickness of the layer is equal to 3 nm (Cinelli et al. 2015, 2017a, b, c, d, e; Einziger et al. 2003). Figure reproduced in Cinelli et al. (2017d)

and Jérusalem et al. (2014), respectively. The piezoelectric effect is only relevant in the through-thickness direction, represented here with orthotropic piezoelectric constants of approximately $1 \text{ nm per } 100 \text{ mV}$ (Zhang et al. 2001) in the thickness direction and zero in the longitudinal and circumferential directions, while the electrical capacitance per unit area changes as the square of the voltage (Cinelli et al. 2017a, b; El Hady et al. 2015).

2.3 Implementation

The head model is implemented as a dynamic analysis in Abaqus CAE (Horgan et al. 2003, 2004) (using Abaqus/Explicit), to allow for the representation of head

impact dynamics and the associated deformation of the brain tissue due to impact.

The nerve bundle model is implemented as a quasi-static analysis in Abaqus CAE 6.13-3, as described in Cinelli et al. (2017a), using Abaqus/Standard. The implementation of the coupled Hodgkin and Huxley (HH) model is shown in Fig. 2 (on the right), and contrasted to the original, uncoupled HH model (on the left) (Cinelli et al. 2017a, c, d). By using the electrothermal equivalence (Cinelli et al. 2017a, c, d), implementation of the coupling between neural activity and the generated strain can be achieved in 3D. The equivalent electrical properties change independently at the nerve membrane of each fibre, based on the spike initiation, strain and voltage generated at the same membrane (Cinelli et al. 2017c, d). In the coupled model (Cinelli et al. 2017d), the mem-

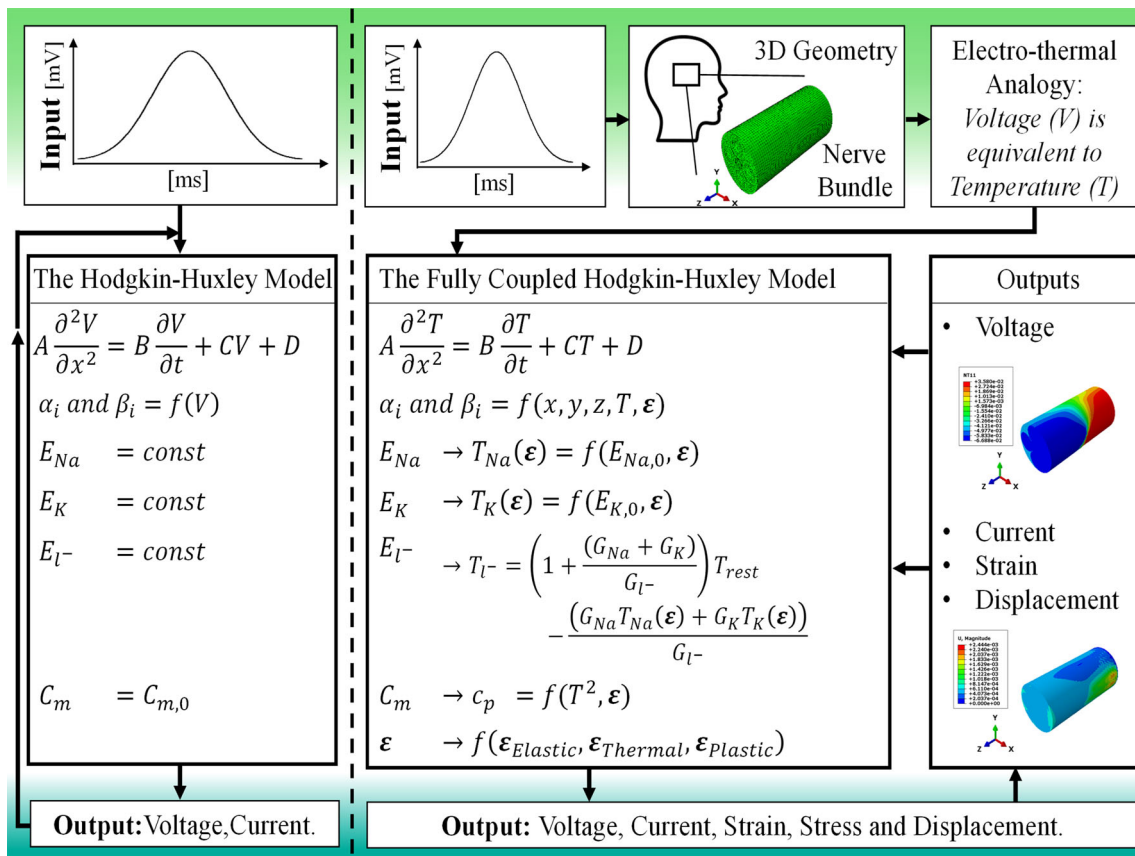


Fig. 3 Flow chart of the code describing the active behaviour of the nerve's membrane: on the left, the HH dynamics (Hodgkin and Huxley 1952) and on the right, the fully coupled HH dynamics. A, B, C and D are general numerical values of specific physical quantities, used to establish the electrothermal equivalences upon which this modelling approach is based (Cinelli et al. 2017c). Here, a Gaussian voltage distribution elicits the action potential in a 3D model of a nervous cell. By using electrothermal equivalences, the HH model is implemented as an equivalent thermal process, in which the membrane's conductivity

changes as in (Hodgkin and Huxley 1952) and the capacitance, C_m , changes as in Cinelli et al. (2017a, d). The HH parameters are changing based on the temperature and strain at the membrane (Cinelli et al. 2017a, b, c). The strain ϵ generated in the model is a function of temperature, T , and thermal expansion coefficients (Cinelli et al. 2017a, b, c). Voltage, current, strain and stresses distribution are only a few of the 3D results released by Abaqus by equivalence. Figure reprinted from Cinelli et al. (2017b)

brane neural activity changes in response to the membrane voltage and total strain (elastic, electrothermal equivalent and plastic), ϵ at the membrane (Hodgkin and Huxley 1952; Jérusalem et al. 2014), while the electrical capacitance per unit area, C_m , changes with the square of the voltage (Cinelli et al. 2017a, b, c); see Fig. 2. The HH resting voltage potentials of sodium, E_{Na} , and potassium, E_K , change due to voltage and strain at the nerve membrane (Boucher et al. 2012; Jérusalem et al. 2014), and hence the threshold of spike initiation changes as prescribed by Hodgkin and Huxley (1952). The reversal potential of the leak ions E_{l^-} is not influenced by the strain but varies based on changes in the gradient concentrations of potassium and sodium across the membrane (Jérusalem et al. 2014). The changes in ion conductance for sodium, G_K , and potassium, G_{Na} , follow the changes in the respective reversal potentials, as in Hodgkin and Huxley (1952) (Fig. 3).

Table 1 shows the parameters used in this model for the steady state and time-varying conditions, and their corresponding value, taken from published experimental literature. Our model accounts for the HH dynamics (Hodgkin and Huxley 1952), implemented by using the thermal analogy of the neural electrical activity in finite element analysis (Cinelli et al. 2017a, c, d). Specific parameters of the ionic reversal potentials vary with the applied strain in time-varying conditions, as described by Jérusalem et al. (2014). Then, due to the variation in thickness (Galbraith et al. 1993; El Hady et al. 2015; Mosgaard et al. 2015; Mueller et al. 2014; Zhang et al. 2001), the membrane capacitance per unit area of a nerve fibre varies as the square of the membrane voltage, V , (Alvarez et al. 1978). More details about the simulation process and formulas, upon which the electromechanical coupling is established, are shown in Cinelli et al. (2017c, d).

Table 1 Parameters of the fully coupled HH dynamics

| Parameters | Symbol | Unit | Formula | Value | References |
|--|-------------------------|--------------------|---|--------|---|
| <i>Steady state</i> | | | | | |
| Ionic reversal potentials | | mV | | | |
| Sodium | $E_{Na,0}$ | | | -115 | Hodgkin and Huxley (1952) |
| Potassium | $E_{K,0}$ | | | 12 | Hodgkin and Huxley (1952) |
| Leak ions | $E_{l,0}$ | | | -10.63 | Hodgkin and Huxley (1952) |
| Ionic conductance | | mS/cm ² | | | |
| Sodium | \bar{g}_{Na} | | | 120 | Hodgkin and Huxley (1952) |
| Potassium | \bar{g}_{K} | | | 36 | Hodgkin and Huxley (1952) |
| Leak ions | \bar{g}_l | | | 0.3 | Hodgkin and Huxley (1952) |
| Membrane capacitance per unit area | $C_m(0)$ | μF/cm ² | | 1 | Hodgkin and Huxley (1952) |
| <i>Time varying</i> | | | | | |
| Ionic reversal potentials | | | | | |
| Sodium | $E_{Na}(\varepsilon_m)$ | | $E_{Na}(\varepsilon_m) = E_{Na0}(1 - (\varepsilon_m/\bar{\varepsilon})^\gamma)$ | | Jérusalem et al. (2014) |
| Potassium | $E_K(\varepsilon_m)$ | | $E_K(\varepsilon_m) = E_{K0}(1 - (\varepsilon_m/\bar{\varepsilon})^\gamma)$ | | Jérusalem et al. (2014) |
| Membrane capacitance per unit area | | μF/cm ² | $C_m(V) = C_m(0)[1 + \vartheta(V + \Delta V)^2]$ | | Alvarez et al. (1978) |
| Strain threshold | $\bar{\varepsilon}$ | % | | 21 | Bain et al. (2000), Jérusalem et al. (2014) |
| Exponential value | γ | | | 2 | Jérusalem et al. (2014) |
| Fractional increase in capacitance per square volt | ϑ | V ⁻² | | 0.036 | Alvarez et al. (1978) |

Depending on the applied boundary conditions, the model is able to simultaneously generate data about the displacement, strain, voltage [equivalent to temperature (Cinelli et al. 2017c)], and stresses (Cinelli et al. 2017c, d). Here, electrical quantities alters mechanical quantities and vice-versa throughout the simulation. This close and simultaneous coupling can be seen over time or at any specific simulation step anywhere in the model. By using this model, the distribution of any generated quantity can be seen in 3D, or can be selected at any specific node or element of any section of the model (here, ECM, ICM or the nerve membrane). Additional quantities can be also released depending on the application. For the purposes of this paper, the strains are

applied at the nerve bundle, see Sect. 2.1, while the voltage is the unknown variable. In previous work, voltage boundary conditions have been used to quantify strain, displacement and stresses (Cinelli et al. 2017c, d).

3 Results

Following a frontal head impact with initial speed v [m/s], the maximum principal value of the nominal strains (NE) [%], found in the white matter region of the head model, vary with v ; see Fig. 4. Although we included large deformation kinematics in the head model, the NE variation is near lin-

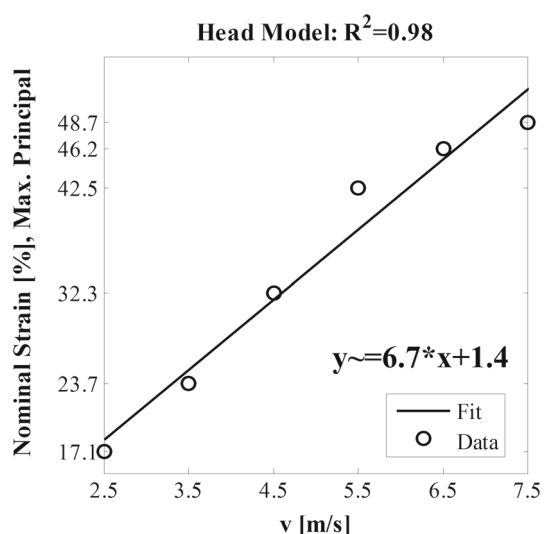


Fig. 4 Variation in the maximum principal value of the nominal strains [%] in the head model versus the speed impact values, v [m/s], used in the frontal head impacts of the head model. Linear regression fit also included

ear. This justifies the investigation of the electrophysiological features of the nerve bundle models based on the quasi-static assumption where only small deformations are considered.

Figure 5 shows the head model, in (a)–(c) and the nerve bundle model in (d)–(i). This figure refers to the case of impact at 7.5 m/s only. The head impacts the floor at 7.5 m/s as shown in (a), where the gravity force is aligned to the z -axis of the head model. At the time of contact with the floor (i.e. 3.75 ms), (b) and (c) show the cerebellum and white matter region of the model, respectively. The contour plots refer to the NE in the head model. From this, the NE in the head model is used to generate the magnitudes of the displacement boundary conditions of the nerve bundle models. Figure 5h, i shows the differences in the mesh and size of the model used for the SB and BB cases in this work. The voltage distribution ($NT11$), equivalent to temperature (Cinelli et al. 2017a, b, c), is shown in (d) for big unmyelinated (BBUN), in (e) for big myelinated (BBMY), in (f) for small unmyelinated (SBUN) and in (g) for small myelinated (SBMY). Here, the voltage refers to the maximum value reached during elongation simulation, in which 48.7% strain determines the magnitude of the displacement boundary condition, see (c), and refers to the case of 7.5 m/s impact, see (a).

Then, the alteration of mechanical and electrical variables of the nerve bundle models is shown in Figs. 6 and 7. The cases of small unmyelinated (SBUN), small myelinated (SBMY), big unmyelinated (BBUN) and big myelinated (BBMY) bundles are considered. A head impact at 2.5 m/s generates a mild-intensity axonal injury at the nerve axon level, because the magnitude of the NE is lower than the threshold considered, 21% (Bain et al. 2000), for initiating

plasticity, and equal to 17.1% (see Fig. 4). In contrast, impacts at 3.5–7.5 m/s generate strains within 23.7–48.7% (beyond the yield strain limit), inducing moderate-intensity axonal injury at the nerve axon level (Bain et al. 2000; Smith et al. 1999). The plastic strain values of the nerve bundle model are permanent strains generated during elongation, and consequently are found to remain after loading (not shown here). Figure 6a, b, d shows that for SBUN, SBMY and BBMY, the magnitude of the maximum principal values of the plastic strain (PE) (%) read at the nerve membrane, have a near-linear relation with the NE found in the head model, and that the PEs vary between 0 and 15%. In contrast, in the BBUN, the PEs are found to be within 0% and 150%, showing a more nonlinear relation with the NE; see Fig. 6c. It is found that bigger bundles undergo larger deformations compared to small bundles and that the myelin sheath has an important role in redistributing the applied strains, preserving the mechanical structure of the fibre (Cinelli et al. 2017a, d). In the BBUN, the entire nerve membrane layer is exposed to the applied deformation during elongation, while, in the BBMY, the myelin sheath protects the Ranvier's node regions from higher deformation by holding up part of the applied strains. Thus, the PEs read at the Ranvier's node regions in BBMY are lower than the PEs found in BBUN.

Figure 7 shows the membrane potential peak and baseline values on Fibre #3 of the nerve bundle models (a)–(c) during loading, and (b)–(d) after loading; values are plotted against the maximum principal value of the NE found in the white matter region of the head model, following impact. In Fig. 7a–c, each point is the peak and baseline voltage, respectively, read at the nerve membrane when the elongation displacement boundary condition is applied on one end of the nerve bundle model. The values are taken at the position where maximum displacement along the fibre middle axis occurs.

The membrane voltage (peak and baseline) changes in relation to the total strains read at the membrane, along the fibre length (Cinelli et al. 2017b) and from the corresponding changes in the ionic reversal potentials (Cinelli et al. 2017a, c, d); see Fig. 3. For total strain lower than 21% (Cinelli et al. 2017a), the ionic reversal potentials vary to produce a different homeostatic ionic gradient across the nerve membrane. For higher strain, the reversal potentials reach a saturation level, simulating loss of charges across the nerve membrane due to permanent deformations at the nerve membrane. This is seen in terms of saturation in membrane voltage levels with increasing NE for all cases except SBUN in Fig. 7a–c.

The voltage differences found during and after elongation, see Fig. 7, arise from the elastic recovery that occurs as soon as the load is removed, while the PEs remain after loading. Results found after loading, shown in (b)–(d), are taken at the same node as during loading for ease of com-

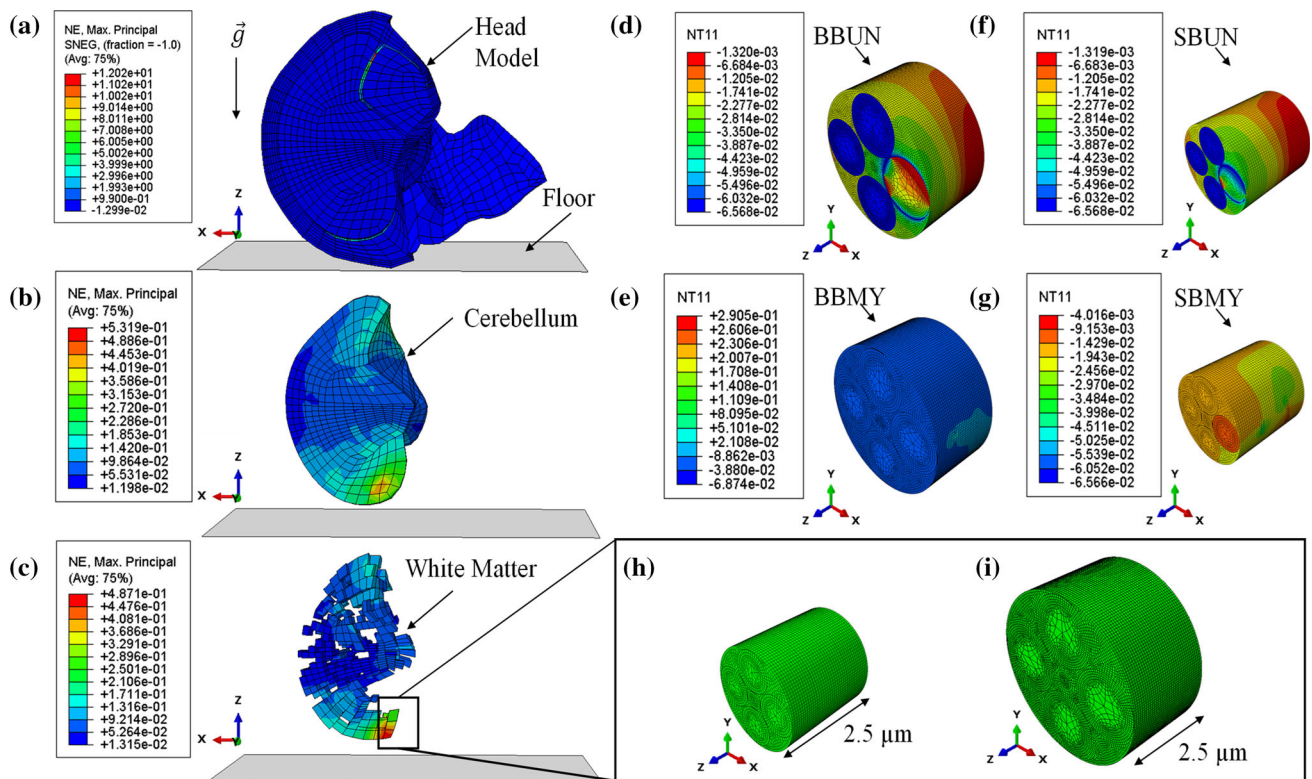


Fig. 5 a–c Head model (Horgan et al. 2003, 2004) and in d–i the nerve bundle model. The head impacts the floor at 7.5 m/s, in a, and, at the instant of contact with the floor, maximum principal nominal strains are shown for the cerebellum, see b, and white matter regions of the head model, see c. A displacement boundary condition is applied to the nerve bundle model with magnitude determined from the maximum value of the strain found in the white matter, see c, for the same case of impact. The voltage (NT11) is equivalent to temperature (Cinelli et al. 2017c, d), and it is shown during elongation at the peak of the

membrane potential. The voltage distribution is shown for: BBUN (d), BBMY (e), SBUN (f) and SBMY (g). In h and i a representation of the mesh and geometry of SB and BB used in this work. The maximum value of each contour plot is reported here in brackets for clarity. For the head model, the maximum of the nominal strain is 12.02, for the cerebellum is 0.5319, and for the white matter is 48.71. Then, peak of the voltage in the BBUN is -1.320 mV, for the BBMY is 0.2905 mV, for the SBUN -1.309 mV and for the SBMY is -4.016 mV

parison. The dashed line refers to the ability of the fibre to generate signals (here, it is found for BBMY only), in contrast with small oscillations of the membrane voltage around the baseline value (solid lines). The levels of oscillation can be deduced by comparing corresponding peak and baseline values, where only the BBMY case shows an appreciable difference both during and after loading; see Fig. 7. Again, the reason is that the myelin sheath layer redistributes the plastic strain around the Ranvier's node regions, and thus the corresponding changes in the ionic reversal potentials are lower than in the other cases. In all cases except the BBUN, there is a general increase in membrane voltage with NE after loading, while the nonlinear variation for BBUN is explained by the nonlinearity in PE (see Fig. 6).

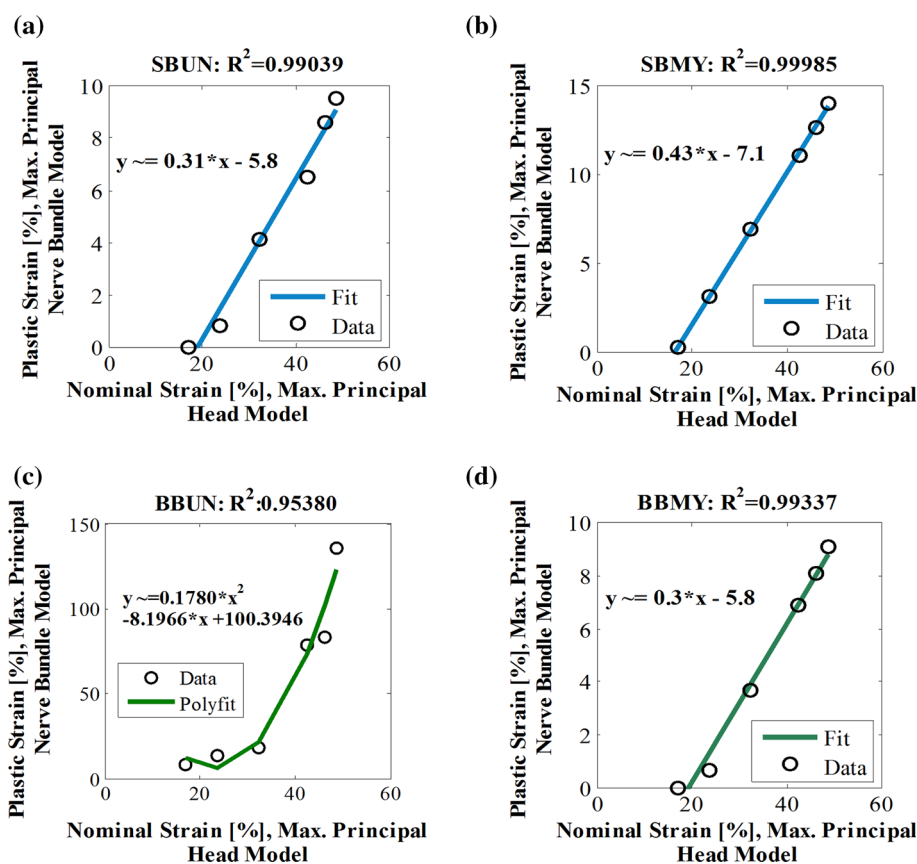
To further illustrate how these results relate to the impact conditions, the supplementary material shows results of PE in the nerve bundle model versus the speed of impact of the head model, and the membrane voltage peak and baseline versus the speed of impact.

4 Discussion

DAI arises from damage of the white matter following TBI (Ma et al. 2016; Wright 2012). The current literature on the subject discusses at length the neurological and non-neurological consequences of DAI (Kan et al. 2012; Lajtha et al. 2009; Smith and Meaney 2000; Wang et al. 2010), the need for need for better diagnosis (Hemphill et al. 2015; Lajtha et al. 2009; Ma et al. 2016; Wright 2012), and the lack of suitable treatments (Hemphill et al. 2015; Lajtha et al. 2009; Wright 2012).

Within this context, computational modelling can be used to simulate complex anatomical and functional damage induced by TBI at different scales, with the goal of improving the understanding of brain injuries and the quality of clinical care. In this work, induced damage following TBI is simulated at the macroscale by using a Head Model (Horgan et al. 2003, 2004), while damage to cellular mechanisms, i.e. the electromechanical impairments of diffuse axonal injury

Fig. 6 Variation in the maximum principal value of the plastic strains [%] in the nerve bundle model, read at the nerve membrane, versus the maximum principal value of the nominal strains [%] in the head model for **a** SBUN, **b** SBMY, **c** BBUN and **d** BBMV. Regression fits also included



(DAI), is simulated by using a nerve bundle model (Cinelli et al. 2017a, b, c, d). The use of two independent, although linked, models is needed to have full control over the applied boundary conditions at the different size scales. Investigation of the structural damage caused by strain levels determined during impact at the macroscale is implemented using an estimation of the plastic strain at the nerve membrane, which is the irrecoverable component of the total strain. The corresponding voltage changes simulated in the nerve bundle model are a measure of the functional damage at the axonal level.

The results show that plastic strains found in the nerve bundle model are linearly related to both the nominal strains generated in the white matter of the Head Model during impact, and the impact speed values themselves; see Figs. 4 and 6. Although large deformation is assumed in the head model, the quasi-static assumption of the nerve bundle model is justified by the linear deformation of the head regions, following impact; see Fig. 4.

By elongating the bundles, it is interesting to note that permanent strains at the membrane are higher in the large unmyelinated bundle, while they are lower than 21% in the other nerve bundle models; see Fig. 6. Following a high-speed frontal head impact, mechanical failure may occur in larger unmyelinated nerve bundles, due to the high plas-

tic strain produced at the membrane; see Figs. 6 and 7a–d. In this work, physical disconnection of fibres within the nerve bundle models (or axotomy (Wang et al. 2011)) is not accounted in the simulation for the range of speeds considered. However, we assume that high plastic strains in the bundle are indicative of disconnection and so, mechanical failure.

Related to this, the functionality of the fibre is also affected by the (axial) component of the total strain, while it also depends on the high number of charges exchanged per unit area (Cinelli et al. 2017a, c, d). The *macro-to-micro*-link allows for analysing the structural and functional failure in nerve bundles with different calibre, following frontal head impacts. Thus, the permanent alterations of the membrane potential are DAI-induced electrical changes that can be linked directly both to the speeds of impact and to the nominal strain of the white matter.

Deforming the bundle, permanent deformations occur at the nerve membrane and at the Ranvier's node regions of unmyelinated and myelinated nerve fibres, respectively, which in turn change the ionic reversal potentials and consequently the homeostatic gradient of the nerve membrane. The shift of the membrane potential to positive values is proportional to the level of stretch applied to the bundle

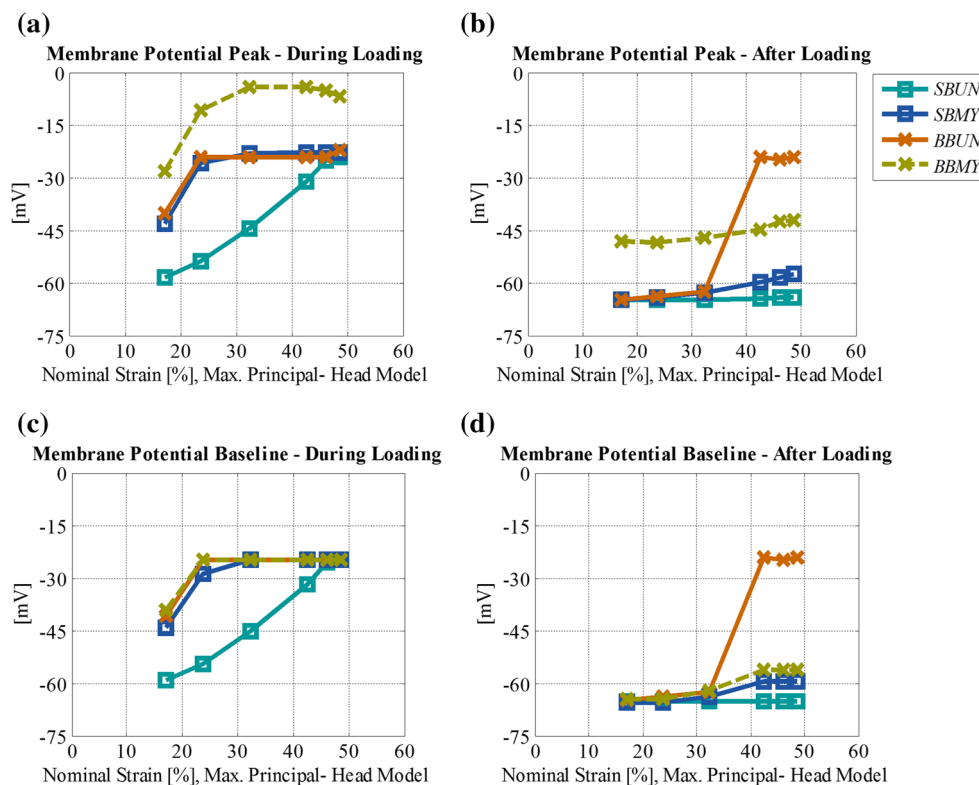


Fig. 7 Membrane potential peak [mV], read at the nerve membrane, versus the maximum principal value of the nominal strains [%] found in the head model; **a** and **c** show the potential values during elongation,

while **b** and **d** show the potential values after elongation. On the top, **a** and **b**, are for the membrane potential peak, read on Fibre #3. On the bottom, **c** and **d**, are for the membrane baseline

(Cinelli et al. 2017d), where the ionic gate channels are physically stretched and kept opened by the applied loads. Due to the magnitude of nominal strains applied (beyond the yield strain limit), these structural and functional changes are not reversible after loading for all the conditions considered here. Small fluctuations of the membrane potential around the voltage baseline could be interpreted as the loss of the ability of the membrane to generate an action potential, thereby leading to functional failure. The use of the *macro-to-micro*-link for analysing functional damage could be thought as an estimation of the cellular functionality following DAI, without the use of invasive devices.

For speed impact values of up to 7.5 m/s, it is found that after loading (i.e. without the elastic component of the total strain) the voltage alterations simulated by the fully coupled Hodgkin and Huxley model (Cinelli et al. 2017d) (see Fig. 3) are shown to be near-linearly related with the nominal strains in the head model for the small bundles (SBUN and SBMY) and big myelinated bundle (BMY). A higher-order relation is needed to describe the nonlinear voltage alterations caused by strain levels beyond the yield strain for the big unmyelinated bundle (BBUN), and for all bundle types during loading.

In contrast to unmyelinated fibres, myelinated fibres preserve the ability to conduct signals even at high deformations

applied to the bundle, because the mechanically induced voltage alterations are significant at the Ranvier node regions only, rather than along the whole fibre length. The myelin layer is thought to protect the fibre (Cinelli et al. 2017a, d) by constraining the deformation at the Ranvier node regions, allowing for a faster recovery of the normal membrane potential baseline value after loading. Therefore, the myelin sheath seems to protect the fibre from mechanical and functional failure. Experimental evidence shows that, the alteration of the membrane potential at the Ranvier's node is not significant due to the myelin sheath layer when a myelinated fibre undergoes rapid stretch at low strain (Gray and Ritchie 1954). Then, functional alteration is observed as conduction block when the applied strain is high enough to induce fibre disconnection (Gray and Ritchie 1954), similarly to the results shown in Fig. 7. Here, the large myelinated bundle is the only bundle type still able to carry a signal after impact, although there is a significant shift in membrane voltage (and therefore change in reversal potentials) during loading.

As seen in experimental studies (Galbraith et al. 1993; Smith et al. 1999; Smith and Meaney 2000), strain rate dependence in elongation is shown to play an important role in understanding damage of axonal cytoskeleton, changes in ionic gating channels and disconnection. Future work can consider further development of the current models to include

strain rate dependence in elongation tests at the cellular level, in addition to rotation and acceleration in head impacts. Finally, the inclusion of a more realistic geometry of the nerve bundle and the inclusion of mechanical anisotropy in the fibre would lead to a more accurate result.

5 Conclusion

This work reports the results of an investigation of electromechanical impairments of DAI, following TBI events of frontal head impacts. The findings of this work could be easily transferable to clinical applications, thanks to the close link between boundary conditions in both models. The main findings can be summarised as:

- At high impact speeds (that cause high nominal strain in the white matter), disconnection of fibres is more likely to occur in large unmyelinated bundles due to the high plastic strains found at the nerve membrane;
- Signal propagation is preserved in the large myelinated bundle;
- There is a linear relation between the generated plastic strain of the nerve bundle model and the impact velocity and the nominal strains of the head model;
- The relation between the membrane voltage peak after loading and the nominal strains in the head model is near-linear in small bundles (regardless of type) and in big myelinated bundles;
- The myelin layer protects the fibre from mechanical failure, preserving its functionalities.

This model can contribute to the understanding of DAI occurrences to improve diagnosis, clinical treatments and prognosis by simulating the mechanical changes accompanying the changes in signal transmission.

5.1 Limitations

In this work, the calibre of the fibres is within the range of small fibres of the human corpus callosum only (Björnholm et al. 2017), as discussed in Cinelli et al. (2017a). As shown in Björnholm et al. (2017) and Kanari et al. (2018), neuronal morphology varies in the nervous system. A wider range of calibre might be accounted in future studies for a more accurate representation of different brain regions and for representing the spatial distribution of mechanical and function failure at microscale through the brain tissue layers (Cinelli et al. 2017a).

Then, for simplicity, the assumption of incompressible rate-independent isotropic mechanical behaviour is chosen for describing the mechanics of nerve bundles (Cinelli et al. 2017a, b, c; El Hady et al. 2015), in contrast to the different

biophysical phenomena chosen for describing the electromechanical coupling and electrical neural activity (Cinelli et al. 2017a, b, c). Thus, this work is not comprehensive enough for replicating viscoelastic behaviour or mechano-sensing properties as observed to occur in nervous cells (Geddes et al. 2003; Kan et al. 2012). A different choice of mechanical properties and calibre might vary the results shown in this paper (Cinelli et al. 2017a).

Acknowledgements The authors gratefully acknowledge funding from the Galway University Foundation, the Biomechanics Research Centre and the Power Electronics Research Centre, College of Engineering and Informatics, NUI Galway (Galway, Republic of Ireland).

Compliance with ethical standards

Conflict of interest The authors declare that the research was conducted in the absence of any commercial or financial relationships that could be construed as a potential conflict of interest.

References

- Abdellah M et al (2018) NeuroMorphoVis: a collaborative framework for analysis and visualization of neuronal morphology skeletons reconstructed from microscopy stacks. *Bioinformatics* 34(13). <https://doi.org/10.1093/bioinformatics/bty231>. Retrieved <https://www.ncbi.nlm.nih.gov/pmc/articles/PMC6022592/pdf/bty231.pdf>
- Alvarez Q et al (1978) Voltage-dependent capacitance in lipid bilayers made from monolayers. *Biophys J.* [https://doi.org/10.1016/s0006-3495\(78\)85505-2](https://doi.org/10.1016/s0006-3495(78)85505-2)
- Bain AC et al (2000) Tissue-level thresholds for axonal damage in an experimental model of central nervous system white matter injury. *J Biomech Eng.* <https://doi.org/10.1115/1.1324667>
- Björnholm L et al (2017) Structural properties of the human corpus callosum: multimodal assessment and sex differences. *NeuroImage.* <https://doi.org/10.1016/j.neuroimage.2017.02.056>
- Boucher PA et al (2012) Coupled left-shift of Nav channels: modeling the Na⁺-loading and dysfunctional excitability of damaged axons. *J Comput Neurosci.* <https://doi.org/10.1007/s10827-012-0387-7>
- Cinelli I et al (2015) Thermo-electrical equivalents for simulating the electro-mechanical behavior of biological tissue. In: *Proceedings of the Annual International Conference of the IEEE Engineering in Medicine and Biology Society, EMBS, vol 2015–Novem*, pp 3969–3972. <https://doi.org/10.1109/EMBC.2015.7319263>
- Cinelli I et al (2017a) Effects of nerve bundle geometry on neurotrauma evaluation. *Int J Numer Methods Biomed Eng.* <https://doi.org/10.1002/cnm.3118>. Retrieved <https://onlinelibrary.wiley.com/doi/full/10.1002/cnm.3118>
- Cinelli I et al (2017b) Electro-mechanical response of a 3D nerve bundle model to mechanical loads leading to axonal injury. In: *Proceedings of the annual international conference of the IEEE Engineering in Medicine and Biology Society, EMBS*, pp 978–81. Retrieved <http://ieeexplore.ieee.org/document/8036989/>
- Cinelli et al (2017c) Electro-thermal equivalent 3D finite element model of a single neuron. *IEEE Trans Biomed Eng* 65(6):1373–1381. <https://doi.org/10.1109/TBME.2017.2752258>. <https://ieeexplore.ieee.org/document/8038069>
- Cinelli et al (2017d) Electro-mechanical response of a 3D nerve bundle model to mechanical loads leading to axonal injury. *Int J Numer*

- Methods Biomed Eng 978–981. <https://doi.org/10.1002/cnm.2942>
- Cinelli I et al (2017e) Neurotrauma evaluation in a 3D electro-mechanical model of a nerve bundle. In: 8th International IEEE EMBS conference on neural engineering, pp 2–5. IEEE. Retrieved <https://ieeexplore.ieee.org/stamp/stamp.jsp?tp=&arnumber=8008402>
- Dixit P et al (2017) A review on recent development of finite element models for head injury simulations. Arch Comput Methods Eng. <https://doi.org/10.1007/s11831-016-9196-x>
- Einzigler PD et al (2003) Novel cable equation model for myelinated nerve fiber. In: First international IEEE EMBS conference on neural engineering, 2003. Conference Proceedings, vol 52(10). <https://doi.org/10.1109/cne.2003.1196769>
- El Hady A et al (2015) Mechanical surface waves accompany action potential propagation. Nat Commun 6(6697). <https://doi.org/10.1038/ncomms7697>. Retrieved <http://www.nature.com/ncomms/2015/150330/ncomms7697/full/ncomms7697.html>
- Galbraith JA et al (1993) Mechanical and electrical responses of the squid giant axon to simple elongation. J Biomech Eng. <https://doi.org/10.1115/1.2895464>
- Garcia-Gonzalez D et al (2017) On the mechanical behaviour of PEEK and HA cranial implants under impact loading. J Mech Behav Biomed Mater. <https://doi.org/10.1016/j.jmbbm.2017.01.012>
- Garcia-Gonzalez D et al (2018) Cognition based BTBI mechanistic criteria; a tool for preventive and therapeutic innovations. Sci Rep. <https://doi.org/10.1038/s41598-018-28271-7>
- Garcia-Grajales JA et al (2015) Neurite, a finite difference large scale parallel program for the simulation of electrical signal propagation in neurites under mechanical loading. PLoS ONE. <https://doi.org/10.1371/journal.pone.0116532>
- Geddes DM et al (2003) Mechanical stretch to neurons results in a strain rate and magnitude-dependent increase in plasma membrane permeability. J Neurotrauma. <https://doi.org/10.1089/089771503770195885>
- Gray JAB, Ritchie JM (1954) Effects of stretch on single myelinated nerve fibres. J Physiol 124(1):84–99. <https://doi.org/10.1113/jphysiol.1954.sp005087>
- Hemphill MA et al (2015) Traumatic brain injury and the neuronal microenvironment: a potential role for neuropathological mechanotransduction. Neuron. <https://doi.org/10.1016/j.neuron.2015.02.041>
- Hodgkin AL, Huxley AF (1952) A quantitative description of membrane current and its application to conduction and excitation in nerve. J Physiol 117(117):500–544. <https://doi.org/10.1007/BF02459568>
- Horgan TJ et al (2003) The creation of three-dimensional finite element models for simulating head impact biomechanics. Int J Crashworthiness. <https://doi.org/10.1533/ijcr.2003.0243>
- Horgan TJ et al (2004) Influence of FE model variability in predicting brain motion and intracranial pressure changes in head impact simulations. Int J Crashworthiness. <https://doi.org/10.1533/ijcr.2004.0299>
- Jérusalem A et al (2014) A computational model coupling mechanics and electrophysiology in spinal cord injury. Biomech Model Mechanobiol 13(4). <https://doi.org/10.1007/s10237-013-0543-7>. Retrieved <http://www.scopus.com/inward/record.url?eid=2-s2.0-84905440293&partnerID=40&md5=ffc79e8dbbf5051ffda14fe185d58>
- Kan EM et al (2012) Microenvironment changes in mild traumatic brain injury. Brain Res Bull. <https://doi.org/10.1016/j.brainresbull.2012.01.007>
- Kanari L et al (2018) A topological representation of branching neuronal morphologies. Neuroinformatics. <https://doi.org/10.1007/s12021-017-9341-1>
- Lajtha et al (2009) Handbook of neurochemistry and molecular neurobiology, vol 281, Springer. <https://doi.org/10.1016/j.jns.2009.03.019>
- Li et al (2016) Epidemiology of traumatic brain injury over the world: a systematic review. General Medicine: Open Access. 04. <https://doi.org/10.4172/2327-5146.1000275>
- Ma J et al (2016) Progress of research on diffuse axonal injury after traumatic brain injury. Neural Plasticity. <https://doi.org/10.1155/2016/9746313>
- Majdan M et al (2016) Epidemiology of traumatic brain injuries in Europe: a cross-sectional analysis. The Lancet Public Health . [https://doi.org/10.1016/s2468-2667\(16\)30017-2](https://doi.org/10.1016/s2468-2667(16)30017-2)
- McCrory P et al (2017) What is the definition of sports-related concussion: a systematic review. Br J Sports Med. <https://doi.org/10.1136/bjsports-2016-097393>
- Mohammadipour A et al (2017) Micromechanical analysis of brain's diffuse axonal injury. J Biomech. <https://doi.org/10.1016/j.jbiomech.2017.09.029>
- Mosgaard LD et al (2015) Mechano-capacitive properties of polarized membranes. Soft Matter 11(40). <https://doi.org/10.1039/c5sm01519g>. Retrieved <http://xlink.rsc.org/?DOI=C5SM01519G>
- Mueller JK et al (2014) A quantitative overview of biophysical forces impinging on neural function. Phys Biol 11(5). <https://doi.org/10.1088/1478-3975/11/5/051001>. Retrieved <http://www.ncbi.nlm.nih.gov/pubmed/25156965>
- Samaka H, Tarlochan F (2013) Finite element (FE) human head models / literature review. Int J Sci Technol Res 2(7):17–31. <https://doi.org/Cranialstudy>
- Siedler DG et al (2014) Diffuse axonal injury in brain trauma : insights from alterations in neurofilaments. Front Cell Neurosci. <https://doi.org/10.3389/fncel.2014.00429>
- Smith DH, Meaney DF (2000) Axonal damage in traumatic brain injury. Neuroscientist. <https://doi.org/10.1177/10738584000600611>
- Smith DH, Wolf JA, Lusardi TA, Lee VM-Y, Meaney DF (1999) High tolerance and delayed elastic response of cultured axons to dynamic stretch injury. J Neurosci 19(11):4263–4269. <https://doi.org/10.1523/JNEUROSCI.19-11-04263.1999>
- Tang-schomer MD et al (2017) Mechanical breaking of microtubules in axons during dynamic stretch injury underlies delayed elasticity, microtubule disassembly, and axon degeneration. FASEB J. <https://doi.org/10.1096/fj.09-142844>
- Wang HC et al (2010) Experimental models of traumatic axonal injury. J Clin Neurosci. <https://doi.org/10.1016/j.jocn.2009.07.099>
- Wang J et al (2011) Traumatic axonal injury in the optic nerve: evidence for axonal swelling. J Neurotrauma. <https://doi.org/10.1089/neu.2011.1756>
- Wazen RM et al (2014) The WU-Minn human connectome project: an overview. NIH Public Access 8(9). <https://doi.org/10.2217/nmm.12.167.gene>. Retrieved <https://www.ncbi.nlm.nih.gov/pmc/articles/PMC3724347/pdf/nihms482605.pdf>
- Wright RM (2012) Computational model for traumatic brain injury based on an axonal injury. The Johns Hopkins University. Retrieved http://media.proquest.com/media/pq/classic/doc/2766607741/fmt/ai/rep/NPDF?_s=g7y7%2F19hqr8ye%2F4816aH5a0IOdo%3D
- Wright RM et al (2012) An axonal strain injury criterion for traumatic brain injury. Biomech Model Mechanobiol. <https://doi.org/10.1007/s10237-011-0307-1>
- Young PG et al (2015) Developing a finite element head model for impact simulation in Abaqus. In: SIMULIA community conference

Yu N et al (2012) Spontaneous excitation patterns computed for axons with injury-like impairments of sodium channels and Na/K pumps. PLoS Comput Biol. <https://doi.org/10.1371/journal.pcbi.1002664>

Zhang PC et al (2001) Voltage-induced membrane movement. Nature 413(6854). <https://doi.org/10.1038/35096578>. Retrieved <http://www.nature.com/nature/journal/v413/n6854/abs/413428a0.html>

Zhang YP et al (2014) Traumatic brain injury using mouse models. Transl Stroke Res. <https://doi.org/10.1007/s12975-014-0327-0>

Publisher's Note Springer Nature remains neutral with regard to jurisdictional claims in published maps and institutional affiliations.

SUPPLEMENTARY MATERIAL

Fig. 8 shows the near-linear relation between the maximum principal value of the plastic strains [%] in the Nerve Bundle Model and the speed impact values, v [m/s], used in the frontal head impacts of the Head Model. These results confirm the trends shown in Fig. 6, providing the equation for each case.

On the active fibre, Fibre #3, during 17.1% of applied elongation, the membrane peak is lower than $-40mV$ for all the bundle types, with the exception of the BBMY where the peak reaches $-29.2 mV$, see Fig. 9 (a). Increasing the elongation up to 23.7 %, a voltage plateau of about $-25 mV$ is reached in the SBMY and BBUN. In contrast, in the BBMY, the voltage plateau is about $-4.02 mV$ at 32.3%, while it is equals to $-24.2 mV$ at 49.7% in SBUN, see Fig.9 (a). In Fig. 9 (c), the voltage baseline is shifted to about $-24 mV$ after 23.7% elongation in the SBMY, BBMY and BBUN, while in the SBUN case the same value is reached after 42.5% elongation. Only in the BBMY, the membrane peaks are distinct from the membrane baseline, see Fig. 9 (a) and (c). After elongation, the membrane voltage peaks vary between $-65 mV$ and $-60 mV$ in both the SBUN and SBMY for all strain values, see Fig. 9 (b). In contrast, in the BBMY, the peaks are about $-45 mV$ for all strains, while, the voltage read in BBUN goes from $-62 mV$ at 32.3 % strain, up to $-24 mV$ at 42.5 – 49.7%, see Fig. 9 (b). A similar trend is found for the voltage baseline, see Fig. 9 (d).

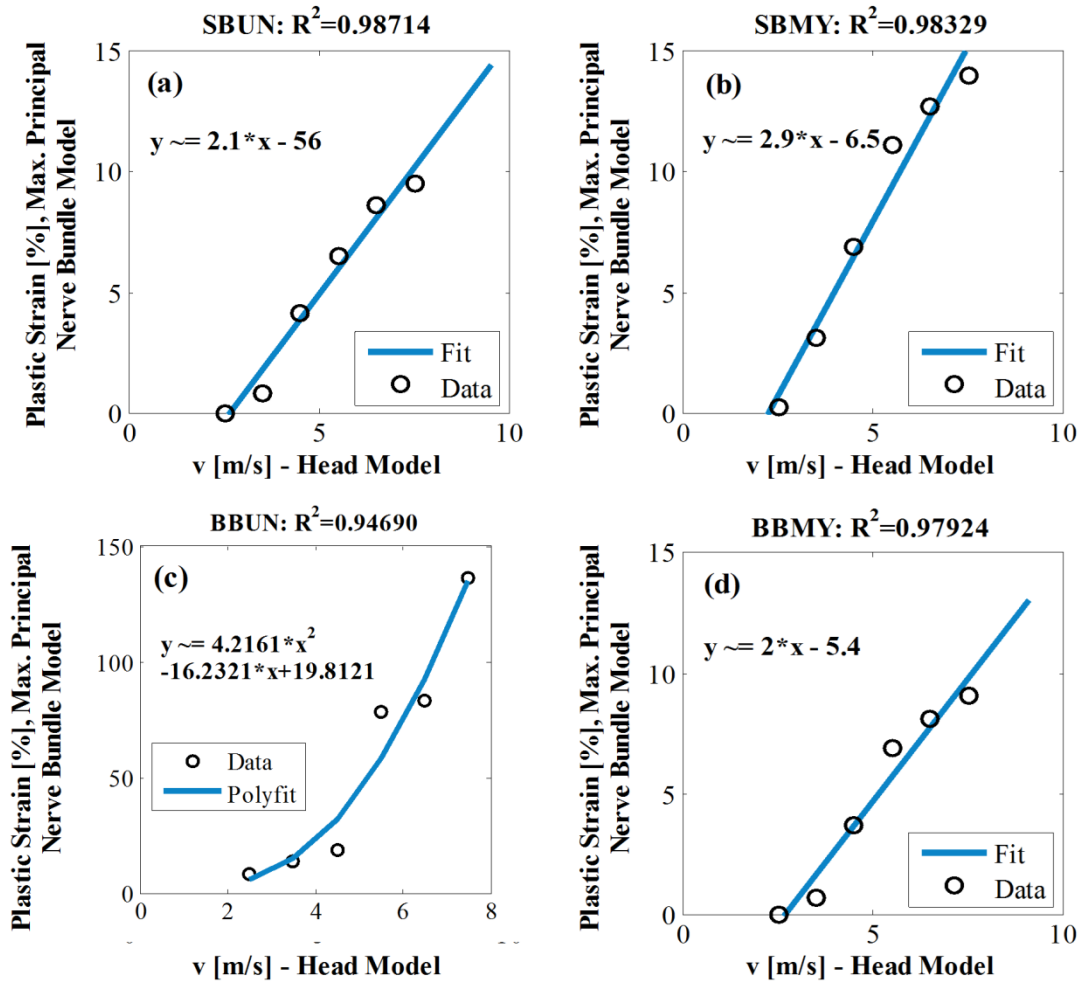


Fig. 8 Variation in the maximum principal value of the plastic strains [%] in the Nerve Bundle Model, read at the nerve membrane, vs. the speed impact values, v [m/s], used in the frontal head impacts of the Head Model. Regression fits are also shown; the fits refer to SBUN, SBMY, BBUN and BBMY in (a) to (d), respectively.

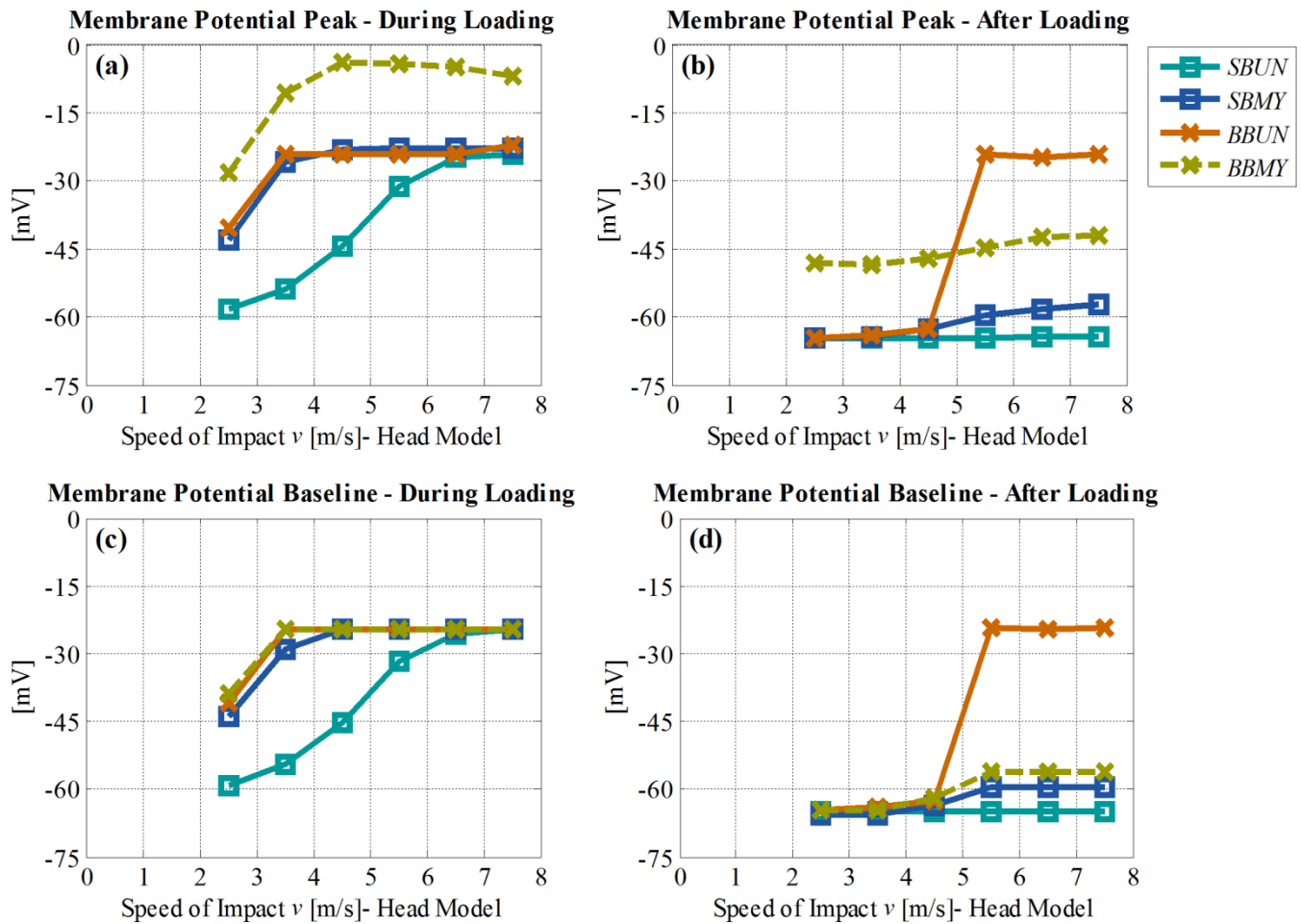


Fig. 9 The membrane potential peak [mv], read at the nerve membrane, vs. the speed of impact values, v [m/s] used in the Head Model; (a) and (c) show the potential values during elongation, while (b) and (d) show the potential values after elongation. On the top, (a) and (b), are for the membrane potential peak, read on Fibre#3. On the bottom, (c) and (d), are for the membrane baseline.